



**HAL**  
open science

## Blend formed by oxygen deficient $\text{MoO}_{3-\delta}$ oxides as lithium-insertion compounds

A.M. Hashem, S.M. Abbas, A.E. Abdel-Ghany, A.E. Eid, A.A. Abdel-Khalek,  
S. Indris, H. Ehrenberg, A. Mauger, C.M. Julien

### ► To cite this version:

A.M. Hashem, S.M. Abbas, A.E. Abdel-Ghany, A.E. Eid, A.A. Abdel-Khalek, et al.. Blend formed by oxygen deficient  $\text{MoO}_{3-\delta}$  oxides as lithium-insertion compounds. *Journal of Alloys and Compounds*, 2016, 686, pp.744-752. 10.1016/j.jallcom.2016.06.043 . hal-01331224

**HAL Id: hal-01331224**

<https://hal.sorbonne-universite.fr/hal-01331224v1>

Submitted on 13 Jun 2016

**HAL** is a multi-disciplinary open access archive for the deposit and dissemination of scientific research documents, whether they are published or not. The documents may come from teaching and research institutions in France or abroad, or from public or private research centers.

L'archive ouverte pluridisciplinaire **HAL**, est destinée au dépôt et à la diffusion de documents scientifiques de niveau recherche, publiés ou non, émanant des établissements d'enseignement et de recherche français ou étrangers, des laboratoires publics ou privés.

**Blend formed by oxygen deficient MoO<sub>3-δ</sub> oxides as lithium-insertion compounds**

A.M. Hashem<sup>1,2</sup>, S.M. Abbas<sup>3</sup>, A.E. Abdel-Ghany<sup>1</sup>, A.E. Eid<sup>1</sup>, A.A. Abdel-Khalek<sup>3</sup>, S. Indris<sup>2</sup>,  
H. Ehrenberg<sup>2</sup>, A. Mauger<sup>4</sup>, C.M. Julien<sup>5</sup>

<sup>1</sup>National Research Centre, Inorganic Chemistry Department, 33 El Bohouth St., (former El Tahrir St.), Dokki-Giza 12622, Egypt

<sup>2</sup>Karlsruhe Institute of Technology (KIT), Institute for Applied Materials –Energy Storage Systems (IAM- ESS), Hermann-von-Helmholtz-Platz 1, D-76344 Eggenstein-Leopoldshafen, Germany

<sup>3</sup>Department of Chemistry, Faculty of Science, Beni-Suef University, Beni-Suef 62111, Egypt

<sup>4</sup>Sorbonne Universités, Univ. UPMC, Paris-6, PHENIX, UMR 8234, 4 place Jussieu, 75005 Paris, France

<sup>5</sup>Sorbonne Universités, Univ. UPMC, Paris-6, IMPMC, 4 place Jussieu, 75005 Paris, France

**Corresponding author:** [christian.julien@upmc.fr](mailto:christian.julien@upmc.fr) (C.M. Julien)

**Keywords:** Molybdenum oxides; Oxygen deficiency; Sol-gel synthesis; Blend; Lithium-insertion compounds

**Abstract**

Oxygen deficient  $\text{Mo}_x\text{O}_y$  200 nm-thick particles were synthesized by a citrate sol-gel method using ammonium heptamolybdate tetrahydrate as a source of Mo and heat treated with a small fraction of zirconia under reducing atmosphere. The samples were investigated by X-ray powder diffraction (XRD), thermal gravimetric analysis (TGA), scanning electron microscope (SEM) and Raman spectroscopy (RS). The structural analyses show that the composite is a blend formed by layered  $\alpha\text{-MoO}_3$ , orthorhombic oxygen deficient phases  $\text{MoO}_{3-\delta}$  with  $\delta=0.25$  ( $\gamma\text{-Mo}_4\text{O}_{11}$ ) and  $\alpha\text{-ZrMo}_2\text{O}_8$ . The insertion of lithium into the lattice was performed by electrochemical method. Redox peaks were observed for the  $\text{MoO}_{3-\delta}$  composite attributed to distinct  $\text{Li}^+$ -ion insertion/extraction reactions in the  $\text{MoO}_3$  and  $\text{Mo}_4\text{O}_{11}$  hosts. The cyclic performance revealed improved reversibility, rate capability, and electrochemical stability of the  $\text{ZrMo}_2\text{O}_8$ -decorated composite with respect to the bare molybdenum oxides. At C/10 rate, the composite delivered a stable reversible capacity of  $135 \text{ mAh g}^{-1}$  after the 50<sup>th</sup> cycle. At a rate of 2C the reversible capacity is maintained at  $118 \text{ mAh g}^{-1}$ , approximately twice the capacity observed for the  $\text{MoO}_3$  particles alone.

## 1. Introduction

MoO<sub>3</sub> is currently investigated for many purposes. Plasmonic MoO<sub>3-x</sub>@MoO<sub>3</sub> nanosheets obtained from surface oxidation of MoO<sub>3-x</sub> were employed as a surface-enhanced Raman scattering (SERS) substrate for methylene blue detection [1]. MoO<sub>3</sub> also enters the composition of solar cells and light-emitting diodes [2,3]. MoO<sub>3</sub> nanoribbons were proposed as a reversible chemochromic material [4]. Redox active polyaniline-h-MoO<sub>3</sub> hollow nanorods [5], ordered mesoporous  $\alpha$ -MoO<sub>3</sub> with iso-oriented nanocrystalline walls [6] and ultrathin MoO<sub>3</sub> nano-crystals self-assembled on graphene nanosheets [7] were proposed as new supercapacitors. It is also applied in the selective conversion of propylene [8]. But MoO<sub>3</sub> is mostly studied for use as an anode material for Li-ion batteries. Recently, single-crystalline  $\alpha$ -MoO<sub>3</sub> nanobelts prepared in 5 M HNO<sub>3</sub> delivered a capacity of 175 mAh g<sup>-1</sup> at the first cycle at 2C rate, falling to 150 mAh g<sup>-1</sup> after 10 cycles, while commercial MoO<sub>3</sub> delivers a stable reversible capacity of 72 mAh g<sup>-1</sup> at 2C rate [9]. To overcome the degradation of MoO<sub>3</sub> nanorod anodes in lithium-ion batteries at high-rate cycling, coating of the nanorods by a protective layer has been proposed. The capacity of  $\alpha$ -MoO<sub>3</sub>-In<sub>2</sub>O<sub>3</sub> core-shell nanorods maintains 1114 and 443 mAh g<sup>-1</sup> after 50 cycles at 0.2C and 2C rate, respectively [10]. Conformal passivation of the surface of MoO<sub>3</sub> nanorods by HfO<sub>2</sub> using atomic layer deposition (ALD) was proposed with success [11]. After 50 charge/discharge cycles at high current density 1500 mA g<sup>-1</sup>, HfO<sub>2</sub>-coated MoO<sub>3</sub> electrodes exhibited a specific capacity of 657 mAh g<sup>-1</sup>. MoO<sub>3</sub> nanoparticles were electrodeposited on Ti nanorod arrays that showed enhanced rate capability (300 mAh g<sup>-1</sup> at 100 A g<sup>-1</sup>) and excellent durability (retaining 300 mA h g<sup>-1</sup> after 1500 cycles at 20 A g<sup>-1</sup>) [12].  $\alpha$ -MoO<sub>3</sub>/multiwalled carbon nanotube (MWCNT) nanocomposite delivered 490 mAh g<sup>-1</sup> at current density 20 A g<sup>-1</sup> owing to the high conductivity of the carbon nanotubes [13]. Porous MoO<sub>3</sub> grafted on TiO<sub>2</sub>

nanotube array was found to improve the specific capacity with respect to MoO<sub>3</sub> alone and the TiO<sub>2</sub> nanotubes alone by a factor three [14]. These results show that MoO<sub>3</sub> shows remarkable electrochemical properties for use as an anode for Li-ion batteries. The price to be paid to obtain such performance, however, is the reduction of the size of the particles to the nano-range, and the synthesis of nano-composites. Such synthesis processes, however, are not scalable, and expensive, which explains that the anode of the commercial Li-ion batteries is still graphitic carbon, although much better results are obtained since years at the laboratory scale, not only with MoO<sub>3</sub> but also with silicon and many metal oxides.

MoO<sub>3</sub> usually exists in three main phases: monoclinic, hexagonal and orthorhombic structure, the later being the most thermodynamically stable phase. Orthorhombic MoO<sub>3</sub> ( $\alpha$ -MoO<sub>3</sub>, n-type semiconductor) attracts interest due to its unique layered structure, which is composed of MoO<sub>6</sub> octahedra in which the Mo atom is surrounded by a distorted oxygen octahedron and connected to another MoO<sub>6</sub> octahedra through edges and corners by covalent and ionic bond, to form double layers [15,16]. The lamellar structure contains extension channels with tetrahedral and octahedral holes suitable for insertion and de-insertion of Li<sup>+</sup> ions [6]. Crystalline  $\alpha$ -MoO<sub>3</sub> has high theoretical discharge capacity of ~370 mAh g<sup>-1</sup>, based on a 2e<sup>-</sup> reduction due a wide range of oxidation states from +4 to +6 [17,18]. The electrochemical behavior of  $\alpha$ -MoO<sub>3</sub> crystals can be described by the redox reaction:



Several methods have been used to prepare nanostructured molybdenum oxides, i.e. hydrothermal synthesis [19,20] electro-spinning method [21], sol-gel technology [22], thin-film deposition [23]. Ette et al. [24] prepared lamellar  $\alpha$ -MoO<sub>3</sub> particles through facile

polymer assisted solvothermal method, and reported good electrochemical performance due to the fast lithium ion diffusion into the lamellar-like morphology.

Non-stoichiometric  $\text{MoO}_{3-\delta}$  oxides with oxygen deficiency [25] are attractive cathode materials for lithium battery application because the excess of metal atoms acts as doping centers, which control the electrical and optical properties [18,26-33].  $\text{MoO}_3$  (Mo as  $\text{Mo}^{6+}$ ) is insulating and transparent with an electronic conductivity  $\sigma < 10^{-8} \text{ S cm}^{-1}$  at  $25^\circ\text{C}$  [32], while the conductivity of  $\text{MoO}_2$  is  $\sigma = 5.0 \times 10^3 \text{ S cm}^{-1}$  [34]. The poor electrical conductivity of  $\alpha\text{-MoO}_3$ , due to the almost ideal stoichiometry, is the major drawback, which severely limits the charge transfer during Li insertion. On another hand, the oxygen deficient  $\text{Mo}_4\text{O}_{11}$  ( $\text{MoO}_{2.75}$ ) exhibits better transport properties with a small electrical resistivity  $\rho = 10^{-4} \Omega \text{ cm}$  and larger average lithium chemical diffusion coefficient of  $\sim 4 \times 10^{-12} \text{ cm}^2 \text{ s}^{-1}$ . In addition, it can accommodate up to 2.1  $\text{Li}^+/\text{Mo}$  in its tunnels without change of the lattice providing a theoretical specific capacity of  $401 \text{ mAh g}^{-1}$  [27]. However, the reversible capacity becomes stable at the level of  $170\text{-}200 \text{ mAh g}^{-1}$  [21].

Recent advances to develop highly effective electrode materials for Li batteries derived from composite or blended architectures, which possess at least two percolating frameworks, for ions and electrons [35]. Numerous examples are cited in the literature:  $x\text{Li}_2\text{MnO}_3 \cdot (1-x)\text{LiMn}_2\text{O}_4$  [36,37], Si/PAN-C [38],  $x\text{LiMnPO}_4 \cdot (1-x)\text{C-LiFePO}_4$  [39],  $\text{Li}_{1.1}\text{Mn}_{1.9}\text{O}_4 \cdot \text{LiNi}_{0.4}\text{Mn}_{0.3}\text{Co}_{0.3}\text{O}_2$  [40],  $\text{LiCoO}_2\text{-LiFePO}_4$  [41]. Depending on the nature and the combination of materials, the blending resulted in different advantages such as: (i) inhibition of overheating effects during overcharge conditions, (ii) reduction of the irreversible capacity decay, (iii) improvement of cycling life and (iv) rise of the accessible discharge C-rate. In addition to the blends, which are physical mixtures, surface modification has been demonstrated to improve the stability and integrity of cathode particles that complement the blending effect [42].

As an effort to alleviate the fading capacity during cycling of the  $\alpha$ - $\text{MoO}_3$  phase, this work presents the study of as-grown blend containing stoichiometric  $\text{MoO}_3$  and oxygen deficient  $\text{Mo}_4\text{O}_{11}$  fabricated through a simple heat treatment of  $\text{MoO}_3$  coated with zirconia in an inert atmosphere. The  $\text{Mo}_4\text{O}_{11}$  phase of the composite provides better transport properties by solving the problem of the poor electronic conductivity of  $\text{MoO}_3$  framework, and by buffering effectively the volume change during cycling. The  $\text{ZrMo}_2\text{O}_8$  decoration is an effective method to preserve the side reactions occurring at the electrolyte-electrode interface that degrade the electrode performance. The samples are investigated by X-ray powder diffraction (XRD), thermal gravimetric analysis (TGA), scanning electron microscope (SEM) and Raman spectroscopy (RS). The structural analyses show that the composite is formed of stoichiometric  $\text{MoO}_3$  and oxygen-deficient phases  $\text{Mo}_4\text{O}_{11}+\text{Mo}_x\text{O}_y$ . The insertion of lithium into the composite is performed by electrochemical methods and compared with that of pristine  $\text{MoO}_3$  and  $\text{Mo}_4\text{O}_{11}$  hosts. Cyclic voltammetry (CV), galvanostatic and electrochemical impedance spectroscopy (EIS) measurements have shown the enhanced transport properties of the composite electrode at the origin of the improvement of the reversible capacity and rate capability.

## 2. Experimental

### 2.1. Synthesis of the composite

Layered  $\text{MoO}_3$  ( $\alpha$ - $\text{MoO}_3$ ) was prepared by a citrate sol-gel method using ammonium molybdate tetrahydrate ( $(\text{NH}_4)_6\text{Mo}_7\text{O}_{24}\cdot 4\text{H}_2\text{O}$ ) as precursor. First, a stoichiometric amount of ammonium molybdate was dissolved in de-ionized water to form an aqueous solution, which was added in a second step to an aqueous solution of citric acid with a 1:1 ratio for metal/chelating agent while stirring gently. The pH values were adjusted to pH=7 using ammonium hydroxide. Then, the sol was obtained by stirring the homogenous mixture for 3 h

in order to favor the complex reaction between the metal ion and the chelating agent. The transparent gel was formed after the slow evaporation of the solution heated at 70 °C. Continuous heating with stirring led to the transformation of the gel to a xerogel, which converted to powder by further drying at ca. 120 °C. The resulting dried precursor was ground and calcined at 500 °C for 5 h in air to obtain MoO<sub>3</sub> single crystals ( $\alpha$ -MnO<sub>3</sub>). The zirconia-coated composite, i.e. oxygen deficient Mo<sub>x</sub>O<sub>y</sub>, was obtained by mixing  $\alpha$ -MnO<sub>3</sub> with Zr(OH)<sub>4</sub> prepared by precipitation of ca. ~4% ZrCl<sub>4</sub> and NaOH dissolved in bi-distilled water. The mixture Zr(OH)<sub>4</sub>+ ( $\alpha$ -MoO<sub>3</sub>) was stirred at room temperature for 3 h, then filtrated, and dried overnight at 60 °C. The final stage to obtain oxygen-deficient blend was a calcination under reduced atmosphere at 500 °C for 5 h in a 5% H<sub>2</sub>/Ar flow

## 2.2. Characterization

Thermogravimetric (TG) measurements were carried out using a thermal gravimetric analyzer (Perkin Elmer, TGA 7 series) in the temperature range of 30–1000 °C in air at a heating rate of 10 °C min<sup>-1</sup>. The structure of the samples was analyzed by X-ray diffraction using a Philips X'Pert apparatus equipped with a CuK $\alpha$  X-ray source ( $\lambda = 1.54056 \text{ \AA}$ ). Data were collected in the  $2\theta$ -range 10–80°. XRD pattern was analyzed by the Rietveld structure refinement program, FULLPROF [43]. The particle morphology of the samples was examined by scanning electron microscope (SEM, JEOL, Japan, JXA-840A). High resolution transmission electron microscopy (HRTEM) analysis was performed using a JEOL TEM2010F at a 200 kV acceleration voltage. For TEM analysis, the powder sample was dispersed on a 3-mm Cu-grid with a hole size of  $1 \times 2 \text{ mm}^2$ . HRTEM and elemental mapping were completed by high-angle annular dark field in a scanning transmission electron microscope (HAADF/STEM) using Emispec ES vision, version 4.0, of the STEM-EDX mapping system. Raman spectra were collected with a double monochromator (Jobin-Yvon

model U1000) using the 514.5 nm line from the Spectra-Physics 2020 Ar-ion laser. The spectra were recorded using a backscattering geometry and the laser power was kept below 25 mW to prevent the degradation of materials upon data acquisition. All spectroscopic data were collected with a spectral resolution of  $2\text{ cm}^{-1}$ .

### 2.3. Electrochemical tests

Electrode materials were prepared by mixing 80% (w/w) of the active material, 10% (w/w) super C65 carbon (TIMCAL) and 10% (w/w) polyvinylidene fluoride (Solef PVdF 6020 binder, Solvay), in N-methyl-2-pyrrolidone (NMP, Sigma-Aldrich) to get a slurry. A  $90\text{ }\mu\text{m}$  thick film was obtained by coating this slurry on aluminum foil that gives an electrode loading  $\sim 7.7\text{ mg cm}^{-2}$ . This film was dried overnight at  $80\text{ }^\circ\text{C}$ , then punched out with the diameter of 1.4 cm. Coin-type cells were assembled in an argon-filled glove box using lithium foil (Alfa Aesar) as anode, LP30 ( $1\text{ mol L}^{-1}\text{ LiPF}_6$  in (1:1) ethylene carbonate (EC) - dimethyl carbonate (DMC) as electrolyte and glass microfiber filters (Whatmann®-GF/D 70 mm  $\varnothing$ ) as separator. VMP3 multi-channel potentiostat (Bio-Logic, France) was used to electrochemically characterize the electrodes at  $25\text{ }^\circ\text{C}$  in the voltage range of 1.5-2.8 V vs.  $\text{Li}^0/\text{Li}^+$  in galvanostatic test and cyclic voltammetry modes.

## 3. Results and discussion

### 3.1. Structure and morphology

Fig. 1a shows the X-ray powder diffraction (XRPD) patterns for the as-prepared pure  $\text{MoO}_3$  ( $\alpha\text{-MoO}_3$ ) and the decorated  $\text{MoO}_3\text{-Mo}_4\text{O}_{11}$  composite sample synthesized under reduced atmosphere. The XRD spectrum of  $\alpha\text{-MoO}_3$  exhibits distinct and sharp peaks attributed to the  $\alpha\text{-MoO}_3$  phase indexed in the orthorhombic structure, *Pbnm* space group (JCPDS card 05-

0508). The lattice parameters  $a=3.993 \text{ \AA}$ ,  $b=13.575 \text{ \AA}$  and  $c=3.713 \text{ \AA}$  were determined using 12 Bragg lines that are in good agreement with values of the literature [15,16]. The XRD diagram of the composite (blend) material shows complex features with the superposition of three sets of Bragg lines. XRD analysis was carried out by Rietveld structure refinement (Fig. 1b), which matches well with the experimental data and gives the composition of the blend sample. The structural data for the modelling were taken from previously reported articles for  $\alpha\text{-MoO}_3$  [15],  $\gamma\text{-Mo}_4\text{O}_{11}$  [45] and  $\alpha\text{-ZrMo}_2\text{O}_8$  [46]. The three phases of low symmetry appear to be with the proportion as follows: (1) an orthorhombic  $\alpha\text{-MoO}_3$  (~65 mol.%) (2) an orthorhombic  $\gamma\text{-Mo}_4\text{O}_{11}$  (30.2 mol.%) and (3) a trigonal  $\alpha\text{-ZrMo}_2\text{O}_8$  (4.8 mol.%). Almost no change is observed in the value lattice parameters of the  $\text{MoO}_3$  component after inert heat-treatment. The appearance of the oxygen deficient oxide  $\text{MoO}_{3-\delta}$  with  $\delta=0.25$  is attributed to a slight reduction of  $\text{MoO}_3$  in hydrogen containing atmosphere [44] that takes part in creation of oxygen vacancies. The non-stoichiometric molybdenum oxide,  $\text{Mo}_4\text{O}_{11}$ , is clearly detected by the presence of XRD peaks located at  $2\theta$  position 20.9, 22.04, 31.9, 34.4 and  $48.2^\circ$ , which match well with database values (JCPDS card 89-6725). The suboxide  $\text{Mo}_4\text{O}_{11}$  can also be written  $(\text{Mo}_3^{6+}\text{Mo}^{4+})\text{O}_{11}$  to outline the two valence states of Mo in it. Kihlberg demonstrated its three-dimensional network based on the  $\text{ReO}_3$ -type structure characterized by the presence of empty channels [25]. The lattice parameters of the  $\gamma\text{-Mo}_4\text{O}_{11}$  phase ( $Pnma$  S.G.) are determined as  $a=24.397 \text{ \AA}$ ,  $b=5.443 \text{ \AA}$ ,  $c=6.732 \text{ \AA}$  that are in agreement with the data in Ref. 6. Therefore,  $\text{Mo}_4\text{O}_{11}$  can be considered as an intermediate phase during the structural change from  $\text{MoO}_3$  to  $\text{MoO}_2$  [44]. The third phase characterized by an additional peak at  $2\theta = 30.54^\circ$  related to trigonal  $\alpha\text{-ZrMo}_2\text{O}_8$  phase ( $P-3c$  S.G.). The structure of the zirconium molybdate is a two-dimensional network with layers perpendicular to the  $c$  axis that is built from  $\text{ZrO}_6$  octahedra linked together by  $\text{MoO}_4$  tetrahedra with unit-cell parameters  $a=10.1391 \text{ \AA}$  and  $c=11.7084 \text{ \AA}$ , which match well with the literature data [47]. The presence of  $\alpha\text{-ZrMo}_2\text{O}_8$

comes from the use of zirconium hydroxide in the synthesis process, which has generated a decoration on the surface of particles. Note that (i) the formation of two molybdate components, i.e.  $\text{Mo}_4\text{O}_{11}$  and  $\text{ZrMo}_2\text{O}_8$  mixed into the blend does alter significantly the lattice parameters of the layered  $\alpha\text{-MoO}_3$  phase, (ii)  $\text{ZrO}_2$  cannot be detected via XRD and (iii) the overall oxygen deficiency of the blend sample was determined by Raman spectroscopy as shown below.

Fig. 2a shows the gravimetric thermogram and the corresponding differential scanning curve (DTG) of the precursor ammonium heptamolybdate tetrahydrate used as the source of Mo and the citric acid used as the chelating agent for the synthesis of  $\alpha\text{-MoO}_3$  by sol-gel method. The thermal behavior in the range 25-950 °C shows stepwise decomposition of the mixture with a total weight loss 71.5 % until the formation of crystalline  $\alpha\text{-MoO}_3$  at 550 °C. The large weight loss occurs in two steps: (i) the loss of water (152 °C) and (ii) the loss of ammonia, combustion of carboxylic acid and acetate xerogel (429 °C) [30]. The thermodynamically stable anhydrous  $\alpha\text{-MoO}_3$  is formed at  $T_c \sim 525$  °C, which is in good agreement with reported values [48]. No change in the weight is observed during heating until the melting point of  $\text{MoO}_3$  at about 795 °C, followed by the decomposition observed as a broad peak in the DTG curve. Fig. 2b displays the TG curve of the Mo-O blend prepared under reduced atmosphere at 500 °C, recorded in air at a rate 10 °C/min. A pronounced increase of weight is observed at  $T > 580$  °C, which is attributed to the oxidation process (gain of oxygen) transforming the blend into the stoichiometric  $\text{MoO}_3$  phase at  $T \approx 600$  °C. Upon further heating, we observed the melt at 780 °C followed by the decomposition of the molybdenum trioxide. Here, the fraction 35% of  $\text{Mo}_4\text{O}_{11}$  is detected from the gain of mass providing the blend composition  $0.65\text{MoO}_3\text{-}0.35\text{Mo}_4\text{O}_{11}$ , a result in agreement with that of Rietveld refinement. Therefore, the presence of a thin  $\text{ZrMo}_2\text{O}_8$  coating is not detected in TG curve, as expected since its melting temperature is known to be as high as 950 °C.

Fig. 3 presents the SEM images of the  $\alpha$ -MoO<sub>3</sub> (a,b) and of the MoO<sub>3</sub>-Mo<sub>4</sub>O<sub>11</sub> blend. The morphology shown in images (3a,3b) reveals well-developed regular slabs of the  $\alpha$ -MoO<sub>3</sub> structure with particles composed of dense packed layers. Image 3a presents the MoO<sub>3</sub> slabs, which form terrace at the edge of particles. The surface morphology of blended sample (images 3c,3d) shows different shapes with irregular rod-like particles typically 10  $\mu$ m thick, decorated with smaller ZrMo<sub>2</sub>O<sub>8</sub> particles (~50 nm), which consists of discontinuous lumps attached to the particle surface.

Fig. 4 illustrates typical HRTEM images and HAADF/STEM mapping of Mo-O blend material. The patterns provide evidence for the structural quality of the sample examined. From the HRTEM image (Fig. 4a) crystal defects (marked by red arrows) of a blend particle are identified, which are attributed to the presence of the two Mo-O phases, i.e. the stoichiometric orthorhombic MoO<sub>3</sub> and the oxygen-deficient orthorhombic Mo<sub>4</sub>O<sub>11</sub> phase. The lattice fringes observed in the HRTEM image are an indicative of orthorhombic structure. The measured lattice fringe spacing 0.37(5) nm corresponds to the (001) crystallographic plane of MoO<sub>3</sub>. The lattice fringes are not uniform and exhibit some discontinuities or misalignment due to the blend architecture of the particle. To determine the local chemical composition, tomography study of the blend phase is shown in the HAADF/STEM image (Fig. 4b). The image of the representative particle used to obtain the elemental analysis is also shown. The images labeled Mn and O, which represent the elemental mapping of the respective elements, are uniform along the shape of the particle examined. Finally, the STEM image (Fig. 4c) displays the MoO<sub>3</sub>-Mo<sub>4</sub>O<sub>11</sub> particles decorated by ZrMo<sub>2</sub>O<sub>8</sub>. The lighter part surrounding the darker particles is the ZrMo<sub>2</sub>O<sub>8</sub> layer, few nm-thick.

Fig. 5 displays the Raman spectra of the  $\alpha$ -MoO<sub>3</sub> and MoO<sub>3</sub>-Mo<sub>4</sub>O<sub>11</sub> blend sample. In the high wavenumber region, the Raman bands observed at 776, 848, and 902 cm<sup>-1</sup> are the

unique spectral features of the  $\alpha$ -MoO<sub>3</sub> orthorhombic phase, especially the 902-cm<sup>-1</sup> peak is assigned as the molybdyl mode, which is the vibration of the terminal Mo=O in the layered structure [38]. The deviation from stoichiometry (i.e. the value of  $x$  in MoO<sub>3-x</sub>) can be determined from the intensity ratio ( $I_{185}/I_{295}$ ) of the Raman bands, i.e. the wagging modes of the terminal Mo=O groups located at 285 and 295 cm<sup>-1</sup> as a function of  $x$  in Fig. 11 of ref. [50]. This deviation from stoichiometry, however is found to be small (the order of 0.5%) for  $\alpha$ -MoO<sub>3</sub>. The much more oxygen-deficient phase in the blend MoO<sub>3</sub>-Mo<sub>4</sub>O<sub>11</sub> is  $x=6\%$ . The Raman pattern of the Mo-O blend displays superposition of both MoO<sub>3</sub> and Mo<sub>4</sub>O<sub>11</sub> components of the blended samples. Seven bands located at 148, 423, 441, 743, 781, 897 and 942 cm<sup>-1</sup> are assigned to the internal modes of the orthorhombic Mo<sub>4</sub>O<sub>11</sub> phase [51]. In addition, small peaks/shoulders pointed out at 177, 326, 360, 751, 885, 943 and 1003 cm<sup>-1</sup> reveal the presence of a small amount of ZrMo<sub>2</sub>O<sub>8</sub>, in good agreement with the XRD results. These Raman peaks are respectively assigned to the lattice mode, the asymmetric and symmetric bending, the asymmetric stretching and the symmetric stretching of MoO<sub>4</sub> tetrahedra [46].

### 3.2. Electrochemical features

Fig. 6 shows the cyclic voltammograms (CV) of  $\alpha$ -MoO<sub>3</sub> (a) and the Mo-O blend (b) samples as positive electrodes in Li coin-type cells. Cycles were performed in the potential range 1.5-3.5 V vs. Li<sup>0</sup>/Li<sup>+</sup> at a scan rate 0.05 mV s<sup>-1</sup>. The CV curve of  $\alpha$ -MoO<sub>3</sub> (Fig. 5a) in the first cycle shows only one anodic peak at 2.55 V, but two cathodic peaks at potentials of 2.70 and 2.30 V vs. Li<sup>0</sup>/Li<sup>+</sup>. These two reduction peaks correspond to consecutive Li<sup>+</sup> ion intercalation processes into the MoO<sub>3</sub> framework: (i) onto sites into the interlayer spacing between the [MoO<sub>6</sub>] octahedral layers (named van der Waals gap) and (ii) onto sites into the slabs, i.e. octahedral intra-layers [52] as illustrated in Fig. 10 of Ref. [53]. The intercalation process

associated with the peak observed at 2.7 V is irreversible, as it is observed only during the first intercalation reaction; this peak vanishes in subsequent cycles. Tsumura and Ingaki [54] reported the irreversible reaction during the first lithiation, which proceeds in a two-phase reaction up to  $\text{Li}_{0.25}\text{MoO}_3$ . The appearance of the  $\alpha\text{-MoO}_3/\text{Li}_x\text{MoO}_3$  system causes a pronounced expansion of the interlayer spacing [55]. The first cycle CV curve for the  $\text{MoO}_3\text{-Mo}_4\text{O}_{11}$  blend (Fig. 5b) appears to be more complex showing the superposition of redox peaks due to each component. The three peaks of  $\text{MoO}_3$  are observed at the same potentials as in the parent material, while three sets of additional peaks are attributed to the  $\text{Mo}_4\text{O}_{11}$  phase: (i) the reversible cathodic peaks at 3.28 and 1.91 V, (ii) reversible anodic peaks at 3.33 and 1.88 V and (iii) irreversible cathodic peaks at 2.45 and 2.20 V vs.  $\text{Li}^0/\text{Li}^+$ . These redox peaks assigned to  $\text{Mo}_4\text{O}_{11}$  are in good agreement with data reported by Besenhard and Schollhorn [56], who noticed trace of reduced Mo suboxide during the reduction process of molybdenum trioxide.

Fig. 7 presents the galvanostatic discharge–charge profiles of the Li coin-type cells cycled at C/10 rate for 50 times, while Figs. 8 (a-b) display the electrochemical performances of Mo-O electrodes. In the first discharge process (lithium intercalation), the discharge–charge curves for  $\alpha\text{-MoO}_3$  (Fig. 7a) and  $\text{MoO}_3\text{-Mo}_4\text{O}_{11}$  blend (Fig. 7b) show two plateaus that correspond to the redox reaction recorded in CV curves. The first irreversible plateau corresponds to an irreversible capacity of  $\sim 50 \text{ mAh g}^{-1}$ . It is observed at about 2.75 V vs.  $\text{Li}^0/\text{Li}^+$  and vanishes in the second and forthcoming cycles. This suggests that part of the  $\text{Li}^+$  ions, first introduced during the reduction reaction (discharge), cannot be extracted. Such an effect has also been observed in  $\text{V}_2\text{O}_5$  [57]. Thus the total intercalation process up to  $1.5\text{Li}^+/\text{Mo}$  can be described as the formation of three phases separated by the bi-phase domain  $\text{MoO}_3\text{-Li}_{0.25}\text{MoO}_3$  that is responsible for voltage plateaus in the first discharge at 2.7 V. The charge-discharge profiles of the Li cell with the  $\text{MoO}_3\text{-Mo}_4\text{O}_{11}$  positive electrode

shows multiple stepwise plateaus at different voltages, associated to the different site occupancies for  $\text{Li}^+$  ions into the framework of each component of the blend. These curves are in good agreement with the data of the cyclic voltammetry. The specific capacity of the  $\alpha\text{-MoO}_3$  in the first discharge is  $250 \text{ mAh g}^{-1}$  and decreases to  $\sim 100 \text{ mAh g}^{-1}$  at the 50<sup>th</sup> cycle, which represents a capacity retention of 37% at rate C/10 (see Figs 7 and 8). The presence of the  $\text{Mo}_4\text{O}_{11}$  phase in the blend improves significantly the electrochemical performance of the electrode. The specific capacity is raised to  $275 \text{ mAh g}^{-1}$  at the first cycle,  $135 \text{ mAh g}^{-1}$  after the 50<sup>th</sup> cycle, both of them being higher than for the  $\text{MoO}_3$  electrode. Our results can be compared with those reported for polyaniline (PANI)/ $\text{MoO}_3$  nanobelt composites synthesized by a hydrothermal method, which exhibited an initial specific capacity  $228 \text{ mAh g}^{-1}$ , but only  $\sim 90 \text{ mAh g}^{-1}$  after 40 cycles at a current density of  $30.7 \text{ mA g}^{-1}$  ( $\sim \text{C}/12$  rate) [58]. The rate capability presented by the modified Peukert plots (Fig. 8a) for the 2<sup>nd</sup> cycle (after the cell formation process and avoid the irreversible loss of capacity associated to the vanishing of the plateau at 2.7 V in Fig. 7) confirms the enhancement in the discharge specific capacity at high C-rate for the  $\text{MoO}_3\text{-Mo}_4\text{O}_{11}$  blended electrode. Typically, at a rate of 2C the capacity is twice that of pure  $\text{MoO}_3$ ; the  $\text{MoO}_3\text{-Mo}_4\text{O}_{11}$  blend electrode retains a capacity of  $118 \text{ mAh g}^{-1}$  against  $60 \text{ mAh g}^{-1}$  for the pure  $\text{MoO}_3$  cathode material.

Fig. 9 presents the EIS results for the  $\text{MoO}_3\text{-Mo}_4\text{O}_{11}$  blended electrode compared with the pristine  $\text{MoO}_3$  material, measured in the frequency range 100 kHz-0.1 Hz with a 5 mV bias. These Nyquist plots show clearly the enhanced transport property of the composite electrode including the  $\text{Mo}_4\text{O}_{11}$  phase. Figs. 9 (a-b) display the electrochemical performances of Mo-O electrodes. This increase in the discharge capacity is attributed to the enhancement of the electronic conductivity of the electrode materials, which can accept higher current densities. These results support the advantage of the Mo-O blend containing the  $\text{Mo}_4\text{O}_{11}$  phase. Stoichiometric  $\text{MoO}_3$  is an insulator with a band gap of 3.1 eV. Oxygen vacancies acts

as doping centers and restores a semiconducting behavior with a conductivity that, however, remains small in  $\text{MoO}_{3-\delta}$ . On another hand,  $\text{Mo}_4\text{O}_{11}$  is a metal (resistivity  $1.66 \cdot 10^{-4} \Omega \text{ cm}$ ) [59]. Since  $\text{Mo}_4\text{O}_{11}$  can be viewed as  $\text{MoO}_3$  that has lost  $\frac{1}{4}$  oxygen per chemical formula, the metallic character of  $\text{Mo}_4\text{O}_{11}$  can be viewed as the result of an insulator to metal Mott transition associated to the increasing concentration of oxygen vacancies. The increase of the electrical conductivity in the blend, as evidenced in Fig. 8, simply gives evidence that the  $\text{Mo}_4\text{O}_{11}$  phase forms an electric conductive network. The increased conductivity and the access to the oxidation states +6, +5 of Mo due to  $\text{Mo}_4\text{O}_{11}$  explains the improvement of the rate capability at  $C > 0.2$  in the blend evidenced in Fig. 8b. The better cycling stability can be attributed to the combination of two effects: (a) the increase of electronic conductivity also makes possible the extraction of a larger amount of lithium. (b) the buffering effect of the non-stoichiometric  $\text{Mo}_4\text{O}_{11}$  component into the blend. (c) the presence of the  $\text{ZrMo}_2\text{O}_8$  decoration protects the electrode from side reaction at the electrolyte-electrode interface.

To our knowledge, this blend is the best result published for molybdenum oxide micron-sized particles so far. As usual better results can be obtained by decreasing the size of the particles to the nano-range. In particular C- $\text{MoO}_3$  porous nanofibers, could deliver a stable reversible capacity of circa  $200 \text{ mAh g}^{-1}$  [21]. This performance, however, is due to the contribution of the carbon to the electrochemical process, and also the contribution of active sites at the porous surface, evidenced by the fact that the capacity at the first cycles was much larger than the theoretical value. Similar remarkable improvements of the electrochemical properties have been obtained by decreasing the size of  $\text{ZrMo}_2\text{O}_8$ -coated particles, such as  $\text{ZrO}_2$ -coated  $\text{Li}_4\text{Ti}_5\text{O}_{12}$  anodes [60], or  $\text{ZrO}_2$ -coated  $\text{LiMn}_2\text{O}_4$  cathodes [61]. The drawback is that such nano-structures have a low density, and their synthesis process is also less scalable than the simple sol-gel process. Nevertheless, the present results suggest that decreasing the

size of the  $\text{ZrMo}_2\text{O}_8$ -decorated  $\text{MoO}_3$ - $\text{Mo}_4\text{O}_{11}$  blend to the nano-range might be promising for applications as electrode of lithium-ion batteries.

#### 4. Conclusions

In this work, we have investigated the structural and electrochemical properties of a blend electrode prepared by self-synthesis of molybdenum oxides creating a suboxide component, which enhances the properties of the physical mixture. The synthetic procedure performed in inert atmosphere with addition of  $\text{Zr}(\text{OH})_4$  provides particles decorated with nanometric zirconium molybdate particles. The structure and morphology of samples were characterized by XRD, TGA, SEM, HRTEM, HAADF/STEM mapping and Raman analyses that show a blend composition  $0.65\text{MoO}_3$ - $0.35\text{Mo}_4\text{O}_{11}$  decorated with  $\text{ZrMo}_2\text{O}_8$  nanoparticles. It is found that both components of the blend are electrochemically active, providing an initial discharge capacity of  $\sim 282 \text{ mAh g}^{-1}$  in the voltage range 1.5-2.8 V vs.  $\text{Li}^0/\text{Li}^+$  larger than that of  $\alpha$ - $\text{MoO}_3$ . We have shown that blending cathode materials results in the minimization of the shortcomings of the parent material,  $\text{MoO}_3$ . We solved the problem of the poor electronic conductivity of  $\text{MoO}_3$  by the fabrication of a Mo-O composite including an oxygen deficient  $\text{MoO}_{3-\delta}$  ( $\delta=0.25$ ) component. Due to the oxygen vacancies, which act as doping centers, the  $\text{MoO}_{3-\delta}$  phase forms an electric conductive network so that the electrochemical performance is enhanced at high C rates. Therefore, the improved electrochemical properties in the  $\text{MoO}_3$ - $\text{Mo}_4\text{O}_{11}$  cell is attributed to two factors: (i) the presence of oxygen vacancies in the  $\text{Mo}_4\text{O}_{11}$  phase that enhances the electrical conductivity of the blend and serves as buffering component to absorb the volume expansion and (ii) the  $\text{ZrMo}_2\text{O}_8$ -decoration that preserves the electrode against side reaction with the electrolyte.

## Acknowledgments

The authors are grateful to Mr. René Villette for his assistance in collecting the HRTEM images and HAADF/STEM mapping.

## References

- [1] X. Tan, L. Wang, C. Cheng, X. Yan, B. Shen, J. Zhang, Plasmonic  $\text{MoO}_{3-x}@\text{MoO}_3$  nanosheets for highly sensitive SERS detection through nanoshell-isolated electromagnetic enhancement. *Chem. Commun.* 52 (2016) 2893-2896.
- [2] K. Majhi, L. Bertoluzzi, K.J. Rietwyk, A. Ginsburg, D.A. Keller, P. Lopez-Varo, A.Y. Anderson, J. Bisquert, A. Zaban, Combinatorial investigation and modeling of  $\text{MoO}_3$  hole-selective contact in  $\text{TiO}_2/\text{Co}_3\text{O}_4/\text{MoO}_3$  all-oxide solar cells. *Adv. Mater. Interfaces* 3 (2016) 1500405.
- [3] K. Banzai, S. Naka, H. Okada,  $\text{MoO}_3/\text{Ag}/\text{MoO}_3$  anode for organic light-emitting diodes and its carrier injection property. *Jpn J. Appl. Phys.* 54 (2015) 054102.
- [4] M. Wang, K.J. Koski, Reversible chemochromic  $\text{MoO}_3$  nanoribbons through zerovalent metal intercalation. *ACS Nano* 9 (2015) 3226-3233.
- [5] V. Kumar, P.S. Lee, Redox active polyaniline-h- $\text{MoO}_3$  hollow nanorods for improved pseudocapacitive performance. *J. Phys. Chem. C* 119 (2015) 9041-9043.
- [6] T Brezesinski, J. Wang, S.H. Tolbert, B. Dunn, Ordered mesoporous  $\alpha\text{-MoO}_3$  with iso-oriented nanocrystalline walls for thin-film pseudocapacitors. *Nat. Mater.* 9 (2010) 146-151.
- [7] K. Zhou, W. Zhou, X. Liu, Y. Sang, S. Ji, W. Li, J. Lu, L. Li, W. Niu, H. Liu, S. Chen, Ultrathin  $\text{MoO}_3$  nanocrystals self-assembled on grapheme nanosheets via oxygen bonding as supercapacitor electrodes of high capacitance and long cycle life. *Nano Energy* 12 (2015) 510-520.

- [8] K. Schuh, W. Kleist, M. Hoj, A. D. Jensen, P. Beato, G. R. Patzke, J.-D. Grunwaldt, Systematic study on the influence of the morphology of  $\alpha$ -MoO<sub>3</sub> in the selective oxidation of propylene. *J. Solid State Chem.* 228 (2015) 42-52.
- [9] B. Han, K.-H. Lee, Y.-W. Lee, S.-J. Kim, H.-C. Park, B.-M. Hwang, D.-H. Kwak, K.-W. Park, mOo“ Nanostructured electrodes prepared via hydrothermal process for lithium ion batteries. *Int. J. Electrochem. Sci.* 10 (2015) 4232 -4240.
- [10] Q. Wang, J. Sun, Q. Wang, D. Zhang, L. Xing, X. Xue, Electrochemical performance of  $\alpha$ -MoO<sub>3</sub>-In<sub>2</sub>O<sub>3</sub> core-shell nanorods as anode materials for lithium-ion batteries. *J. Mater. Chem. A* 3 (2015) 5083-5091.
- [11] B. Ahmed, M. Shahid, D.H. Nagaraju, D.H. Anjum, M.N. Hedhili, H.N. Alshareef, Surface passivation of MoO<sub>3</sub> nanorods by atomic layer deposition toward high rate durable Li ion battery anodes. *ACS Appl. Mater. Interfaces* 7 (2015) 13154-13163.
- [12] G. Zhao, C. Li, L. Zhang, J. Lv, Y. Niu, Y. Du, K. Sun, « Sea cucumber »-like Ti@MoO<sub>3</sub> nanorod arrays as self-supported lithium ion battery anodes with enhanced rate capability and durability. *J. Mater. Chem. A* 3 (2015) 22547-22551.
- [13] F. Ma, A. Yuan, J. Xu, P. Hu, Porous  $\alpha$ -MoO<sub>3</sub>/MWCNT nanocomposite synthesized via a surfactant-assisted solvothermal route bas a lithium-ion battery high capacity anode material with excellent rate capability and cyclability. *ACS Appl. Mater. Interfaces* 7 (2015) 15531-15541.
- [14] A. Tauseef, W. Li, J. Li, C. Wang, S. R. Ur Rehman, T. Liang, Lithium storage study on MoO<sub>3</sub>-grafted TiO<sub>2</sub> nanotube arrays. *Appl. Nanoscience* (2016) DOI: 10.1007/s13204-016-0526-y.
- [15] S. Anderson, A. Magnelli, Structure of MoO<sub>3</sub>. *Acta Chem. Scand.* 4 (1950) 793-799.
- [16] L. Kihlberg, Studies on molybdenum oxides. *Acta Chem. Scand.* 13 (1959) 954-962.

- [17] C.M. Julien, A. Mauger, A. Vijn, K. Zaghbi, Lithium batteries, science and technology, Springer, Cham, Switzerland (2016) pp 120-124.
- [18] C. Julien, A. Yebka, Electrochemical features of lithium batteries based on molybdenum-oxide compounds. NATO-Science Ser. 85 (2000) 263-277.
- [19] B. Gao, H. Fan, X. Zhang, Hydrothermal synthesis of single crystal  $\text{MoO}_3$  nanobelts and their electrochemical properties as cathode electrode materials for rechargeable lithium batteries. J. Phys. Chem. Solids 73 (2012) 423-429.
- [20] V.M. Mohan, W. Chen, K. Murakami, Synthesis, structure and electrochemical properties of polyaniline/ $\text{MoO}_3$  nanobelt composite for lithium battery. Mater. Res. Bull. 48 (2013) 603-608.
- [21] C. Feng, H. Gao, C. Zhang, Z. Guo, H. Liu, Synthesis and electrochemical properties of  $\text{MoO}_3/\text{C}$  nanocomposite. Electrochim. Acta 93 (2013) 101-106.
- [22] A.K. Prasad, D.J. Kubinski, P.I. Gouma, Comparison of sol-gel and ion beam deposited  $\text{MoO}_3$  thin film gas sensors for selective ammonia detection. Sens. Actuators B 93 (2003) 25-30
- [23] C. Julien, O.M. Hussain, L. El-Farh, M. Balkanski, Electrochemical studies of lithium insertion in  $\text{MoO}_3$  films. Solid State Ionics 53-56 (1992) 400-404.
- [24] P.M. Ette, P. Gurunathan, K. Ramesha, Self-assembled lamellar alpha-molybdenum trioxide as high performing anode material for lithium-ion batteries. J Power Sources 278 (2015) 630-638.
- [25] S. Asbrink, L. Kihlberg L, A study of the crystal symmetry and structure of orthorhombic  $\text{Mo}_4\text{O}_{11}$  by least-squares techniques. Acta Chem. Scand. 18 (1964) 1571-1573.

- [26] P. Cignini, M. Icovi, S. Panero, G. Pistoia, C. Temperoni, Non-Stoichiometric molybdenum oxides as cathodes for lithium cells. Part I. Primary batteries. *J. Electroanal. Chem.* 102 (1979) 333-341.
- [27] M. Icovi, S. Panero, A. D'Agate, G. Pistoia, C. Temperoni, Non-Stoichiometric molybdenum oxides as cathodes for lithium cells. Part II. Secondary batteries. *J. Electroanal. Chem.* 102 (1979) 343-349.
- [28] G. Pistoia, C. Temperoni, P. Cignini, M. Icovi, S. Panero, Non-Stoichiometric molybdenum oxides as cathodes for lithium cells. Part III: Cells based on  $\text{Mo}_{18}\text{O}_{52}$ . *J. Electroanal. Chem.* 108 (1980) 169-180.
- [29] H. Ohtsuka, Y. Sakurai, Characterization of  $\text{MoO}_{3-x}$  thin films. *Jpn J. Appl. Phys.* 40 (2001) 4680-4683.
- [30] S.S. Sunu, E. Prabhu, V. Jayaraman, K.I. Gnanasekar, T.K. Seshagiri, T. Gnanasekaran, Electrical conductivity and gas sensing properties of  $\text{MoO}_3$ . *Sens. Actuators B* 101 (2004) 161-174.
- [31] L. Ben-Dor, Y. Shimony, Crystal structure, magnetic susceptibility and electrical conductivity of pure and NiO-doped  $\text{MoO}_2$  and  $\text{WO}_2$ . *Mater. Res. Bull.* 9 (1974) 837-844.
- [32] V.P. Tysyachny, E.M. Shembel, R.D. Apostolova, V.M. Nagirny, K.E. Kylyvnyk, N.I. Eskova, Studies of the lithium ion transport properties in electrolytic molybdenum oxides, *Solid State Ionics* 169 (2004) 135-137.
- [33] C. Julien, G.A. Nazri Transport properties of lithium-intercalated  $\text{MoO}_3$ . *Solid State Ionics* 68 (1994) 111-116.
- [34] Y. Zhao, Y. Zhang, Z. Yang, Y. Yan, K. Sun, Synthesis of  $\text{MoS}_2$  and  $\text{MoO}_2$  for their applications in  $\text{H}_2$  generation and lithium ion batteries: a review. *Sci. Technol. Adv. Mater.* 14 (2013) 043501.

- [35] S.B. Chikkannanavar, D.M. Bernardi, L. Liu, A review of blended cathode materials for use in Li-ion batteries. *J. Power Sources* 248 (2014) 91-100.
- [36] M.M. Thakeray, C.S. Johnson, J.T. Vaughey, N. Li, S.A. Hackney, Advances in manganese-oxide composite electrodes for lithium-ion batteries. *J. Mater. Chem.* 15 (2005) 2257-2267.
- [37] J. Gao, A. Manthiram, Eliminating the irreversible capacity loss of high capacity layered  $\text{Li}[\text{Li}_{0.2}\text{Ni}_{0.13}\text{Mn}_{0.54}\text{Co}_{0.13}]\text{O}_2$  cathode by blending with other lithium insertion hosts. *J. Power Sources* 191 (2009) 644-647.
- [38] M.K. Datta, P.N. Kumta, Silicon and carbon based composite anodes for lithium ion batteries. *J. Power Sources* 158 (2006) 557-563.
- [39] K. Zaghbi, M. Trudeau, A. Guerfi, J. Trottier, A. Mauger, C.M. Julien, New advanced cathode material:  $\text{LiMnPO}_4$  encapsulated with  $\text{LiFePO}_4$ . *J. Power Sources* 204 (2012) 177-181.
- [40] H. Kitao, T. Fujihara, K. Takeda, N. Nakanishi, T. Nohma, High-temperature storage performance of Li-ion batteries using a mixture of Li-Mn spinel and Li-Ni-Co-Mn oxide as a positive electrode material. *Electrochem. Solid-State Lett.* 8 (2005) A87-A90.
- [41] N. Imachi, Y. Takano, H. Fujimoto, Y. Kida, S. Fujitami, Layered cathode for improving safety of Li-ion batteries. *J. Electrochem. Soc.* 154 (2007) A412-A416.
- [42] A. Mauger, C.M. Julien, Surface modifications of electrode materials for lithium-ion batteries: status and trends. *Ionics* 20 (2014) 751-787.
- [43] J.R. Carjaval, Recent advances in magnetic structure determination by neutron powder diffraction. *Phys. B* 192 (1993) 55-69.
- [44] M.A. Camacho-Lopez, L. Escobar-Alarcon, M. Picquart, R. Arroyo, G. Cordoba, E. Haro-Poniatowski, Micro-Raman study of the  $m\text{-MoO}_2$  to  $\alpha\text{-MoO}_3$  transformation induced by cw-laser irradiation. *Opt. Mater.* 33 (2011) 480-484.

- [45] E. Canadell, M.H. Whangbo, C. Schlenker, C. Escribe-Filippini, Band electronic structure study of the electronic instability in the Magneli phase molybdenum oxide ( $\text{Mo}_4\text{O}_{11}$ ). *Inorg. Chem.* 28 (1989) 1466-1472.
- [46] D.V.S. Muthu, B. Chen, J.M. Wrobel, A.M. Krogh-Andersen, S. Carlson, M.B. Kruger, Pressure-induced phase transitions in  $\alpha\text{-ZrMo}_2\text{O}_8$ . *Phys. Rev. B* 65 (2002) 064101.
- [47] S. Carlson, A.M.K. Andersen, High-pressure transitions of trigonal  $\alpha\text{-ZrMo}_2\text{O}_8$ . *Phys. Rev. B* 61 (2000) 11209-11212.
- [48] P. Roman, A. Luque, A. Aranzabe, Synthesis of oxides, oxocarbides and carbides of molybdenum by thermal decomposition of diethylenetriamine oxomolybdenum compounds. *Thermochim. Acta* 223 (1993) 167-175.
- [49] G.A. Nazri, C. Julien, Far-infrared and Raman studies of orthorhombic  $\text{MoO}_3$  single crystal. *Solid State Ionics* 53 (1992) 376-382.
- [50] M. Dieterle, G. Weinberg, G. Mestl, Raman spectroscopy of molybdenum oxides. Part I. Structural characterization of oxygen defects in  $\text{MoO}_{3-x}$  by UV/VIS, Raman spectroscopy and X-ray diffraction. *Phys. Chem. Chem. Phys.* 4 (2002) 812-821.
- [51] M. Dieterle, G. Mestl, Raman spectroscopy of molybdenum oxides. Part II. Resonance Raman spectroscopic characterization of the molybdenum oxides  $\text{Mo}_4\text{O}_{11}$  and  $\text{MoO}_2$ . *Phys. Chem. Chem. Phys.* 4 (2002) 822-826.
- [52] J.S. Chen, Y.L. Cheah, S. Madhavi, X.W. Lou, Fast synthesis of alpha- $\text{MoO}_3$  nanorods with controlled aspect ratios and their enhanced lithium storage capabilities. *J. Phys. Chem. C* 114 (2010) 8675-8678.
- [53] A.M. Hashem, H. Groult, A. Mauger, K. Zaghib, C.M. Julien, Electrochemical properties of nanofibers  $\alpha\text{-MoO}_3$  as cathode materials for Li batteries. *J. Power Sources* 219 (2012) 126-132.

- [54] T. Tsumura, M. Inagaki, Lithium insertion/extraction reaction on crystalline  $\text{MoO}_3$ . *Solid State Ionics* 104 (1997) 183-189.
- [55] A.M. Hashem, M.H. Askar, M. Winter, J.H. Albering, J.O. Besenhard, Two-phase reaction mechanism during chemical lithium insertion into  $\alpha\text{-MoO}_3$ . *Ionics* 13 (2007) 3-8.
- [56] J.O. Besenhard, R. Schollhorn, The discharge reaction mechanism of the  $\text{MoO}_3$  electrode in organic electrolyte. *J. Power Sources* 1 (1976-1977) 267-276.
- [57] F. Leroux, B.E. Loene, L.F. Nazar, Electrochemical lithium intercalation into a polyaniline/ $\text{V}_2\text{O}_5$  nanocomposite. *J. Electrochem. Soc.* 143 (1996) L181-L183.
- [58] V.M. Mohan, W. Chen, K. Murakami, Synthesis, structure and electrochemical properties of polyaniline/ $\text{MoO}_3$  nanobelt composite for lithium battery. *Mater. Res. Bull.* 48 (2013) 603-608.
- [59] M. C. Rao, K. Ravindranadh, A. Kasturi, M. S. Shekhawat, Structural Stoichiometry and Phase Transitions of  $\text{MoO}_3$  thin films for solid state micro-batteries. *Research J. Recent Research* 2 (2004) 67-73.
- [60] J. Liu, X. Li, M. Cai, R. Li, X. Sun, Ultrathin layer deposited  $\text{ZrO}_2$  coating to enhance the electrochemical performance of  $\text{Li}_4\text{Ti}_5\text{O}_{12}$  as anode. *Electrochim. Acta* 93 (2013) 195-201.
- [61] J. Zhao, Y. Wang, Atomic layer deposition of epitaxial  $\text{ZrO}_2$  coating on  $\text{LiMn}_2\text{O}_4$  nanoparticles for high-rate lithium ion batteries at elevated temperature. *Nano Energy* 2 (2013) 882-889.

**Figure captions**

Fig. 1. (a) X-ray powder diffraction for pure  $\text{MoO}_3$  prepared by sol-gel method and zirconia coated composite calcined in reduced atmosphere. (b) Rietveld refinement of the XRD data of the  $\text{ZrMo}_2\text{O}_8$  decorated  $\text{MoO}_3$ - $\text{Mo}_4\text{O}_{11}$  composite.

Fig. 2. (a) TGA and DTG curves of the precursor showing the crystallization and decomposition of  $\alpha$ - $\text{MoO}_3$  in air with heating rate  $10\text{ }^\circ\text{C}/\text{min}$ . (b) TGA curve of the blend  $\text{MoO}_3$ - $\text{Mo}_4\text{O}_{11}$  showing the oxidation of the suboxide component at  $580\text{ }^\circ\text{C}$ .

Fig. 3. SEM images of  $\alpha$ - $\text{MoO}_3$  (a,b) and  $\text{MoO}_3$ - $\text{Mo}_4\text{O}_{11}$  blend decorated by  $\text{ZrMo}_2\text{O}_8$  (c,d).

Fig. 4. (a) HRTEM image of Mo-O blend material showing the crystal defects (marked by red arrows) that are induced by the presence of stoichiometric  $\text{MoO}_3$  and oxygen-deficient  $\text{Mo}_x\text{O}_y$  phases in the particle. (b) HAADF/STEM mapping and (c) STEM image showing the  $\text{ZrMo}_2\text{O}_8$  phase surrounding the core of blend Mo-O particles.

Fig. 5. Raman spectra of the orthorhombic  $\alpha$ - $\text{MoO}_3$  and  $\text{ZrMo}_2\text{O}_8$ -decorated Mo-O blend. Samples were excited at a laser wavelength of  $514.5\text{ nm}$ .

Fig. 6. Cyclic voltammograms of  $\alpha$ - $\text{MoO}_3$  (a) and  $\text{MoO}_3$ - $\text{Mo}_4\text{O}_{11}$  blend (b) recorded at  $0.05\text{ mV s}^{-1}$  in the potential range  $1.5$ - $3.5\text{ V vs. Li}^0/\text{Li}^+$  in Li cell using  $1\text{ mol L}^{-1}\text{ LiPF}_6$  in EC:DEC electrolyte.

Fig. 7. Charge-discharge profiles as a function of cycles of Li coin-type cells including (a)  $\alpha$ - $\text{MoO}_3$  and (b)  $\text{MoO}_3$ - $\text{Mo}_4\text{O}_{11}$  blend as cathode materials. Measurements were carried out at C/10 rate in the voltage range 1.5-2.8 V vs.  $\text{Li}^0/\text{Li}^+$ .

Fig. 8. Electrochemical performance of Li cells with  $\alpha$ - $\text{MoO}_3$  and  $\text{MoO}_3$ - $\text{Mo}_4\text{O}_{11}$  blend electrodes: (a) rate capability at the second cycle (the rate is denoted C/n, where C is the theoretical cathode capacity and a full discharge occurs in n hours) and (b) cycling performance at rate C/10.

Fig. 9. Nyquist plots of (a)  $\alpha$ - $\text{MoO}_3$  and (b)  $\text{MoO}_3$ - $\text{Mo}_4\text{O}_{11}$  blend as cathode materials. Measurements were carried out in the frequency range 100 kHz-0.1 Hz with a 5 mV bias. Values are frequencies in Hz.

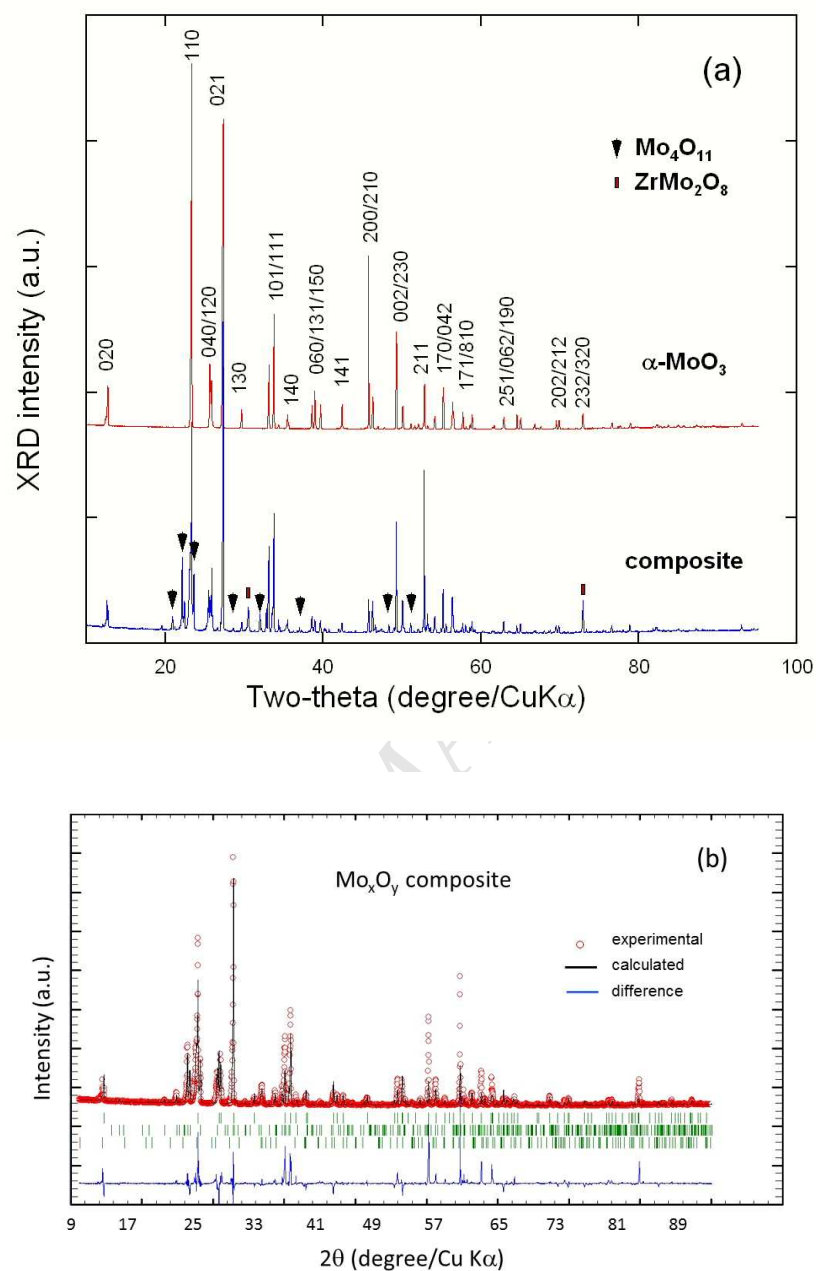


Figure 1. (a) X-ray powder diffraction for  $\alpha$ -MoO<sub>3</sub> prepared by sol-gel method and zirconia coated composite calcined in reduced atmosphere. (b) Rietveld refinement of the XRD data of the ZrMo<sub>2</sub>O<sub>8</sub> decorated MoO<sub>3</sub>-Mo<sub>4</sub>O<sub>11</sub> composite.

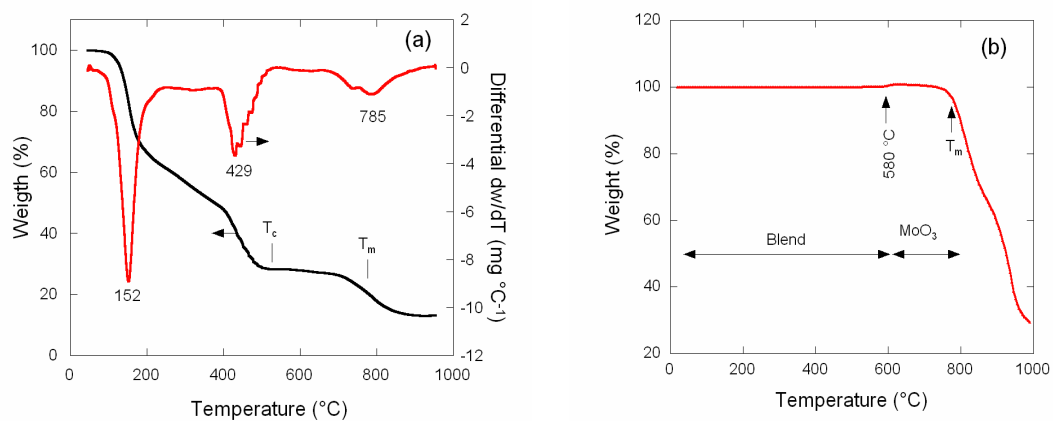


Figure 2. (a) TGA and DTG curves of the precursor showing the crystallization and decomposition of  $\alpha$ -MoO<sub>3</sub> in air with heating rate 10 °C/min. (b) TGA curve of the blend MoO<sub>3</sub>-Mo<sub>4</sub>O<sub>11</sub> showing the oxidation of the suboxide component at 580 °C.

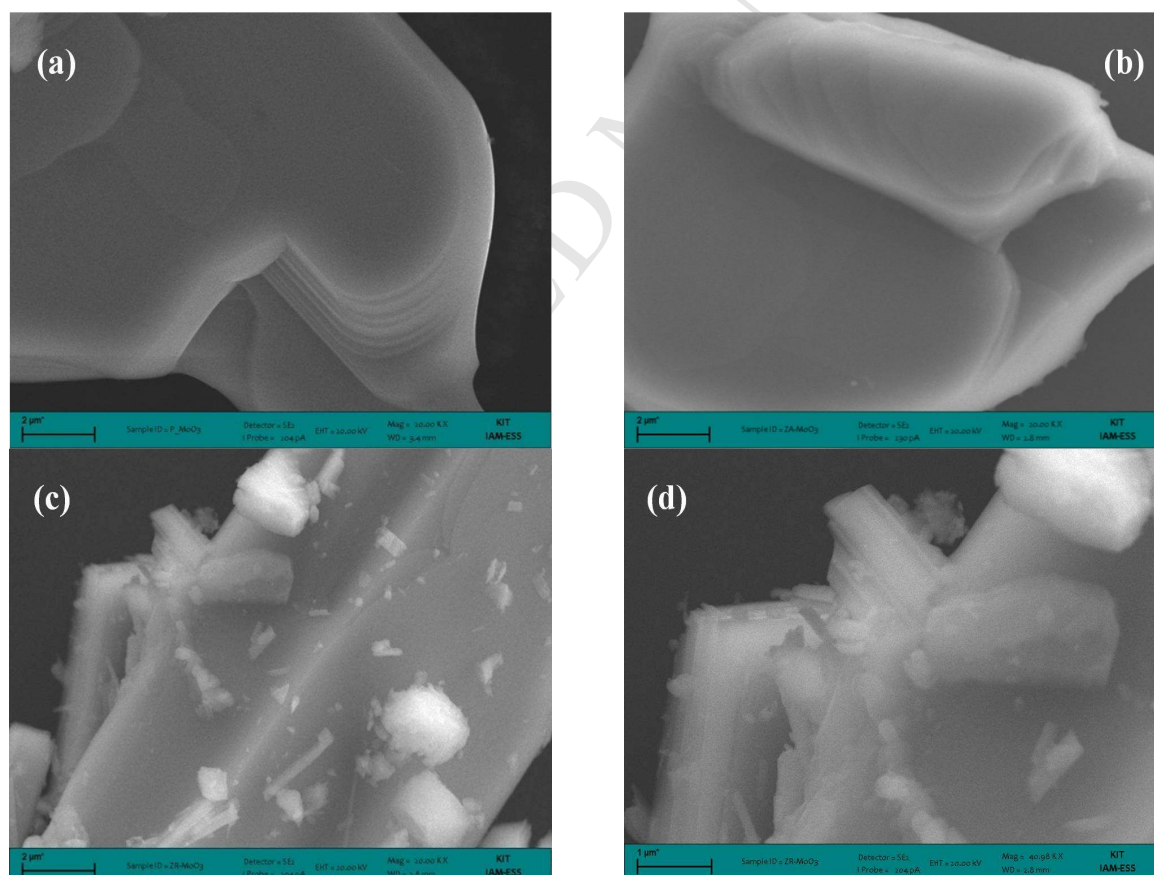


Figure 3. SEM images of  $\alpha$ -MoO<sub>3</sub> (a,b) and MoO<sub>3</sub>-Mo<sub>4</sub>O<sub>11</sub> blend decorated by ZrMo<sub>2</sub>O<sub>8</sub> (c,d).

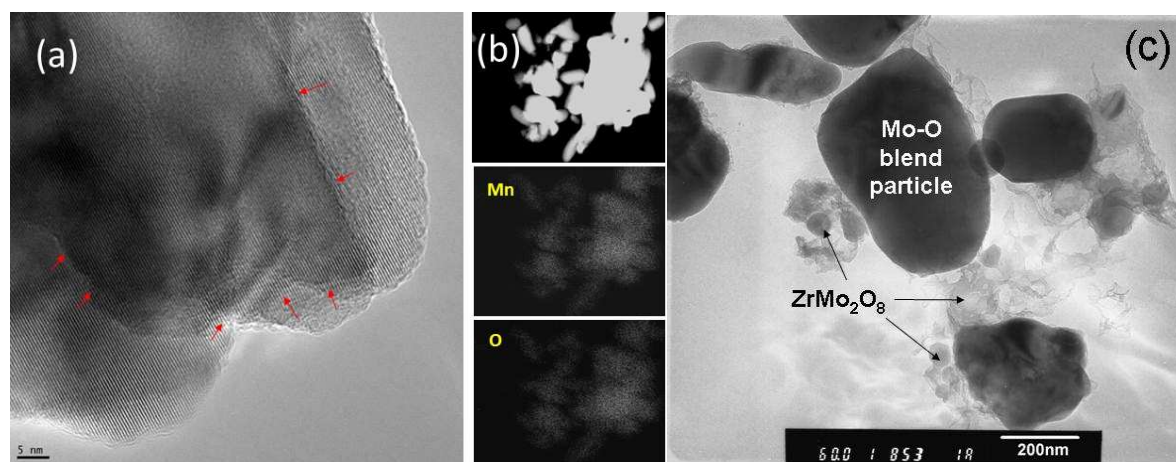


Figure 4. (a) HRTEM image of Mo-O blend material showing the crystal defects (marked by red arrows) that are induced by the presence of  $\alpha$ -MoO<sub>3</sub> and oxygen-deficient Mo<sub>x</sub>O<sub>y</sub> phases in the particle. (b) HAADF/STEM mapping and (c) STEM image showing the ZrMo<sub>2</sub>O<sub>8</sub> phase surrounding the core of blend Mo-O particles.

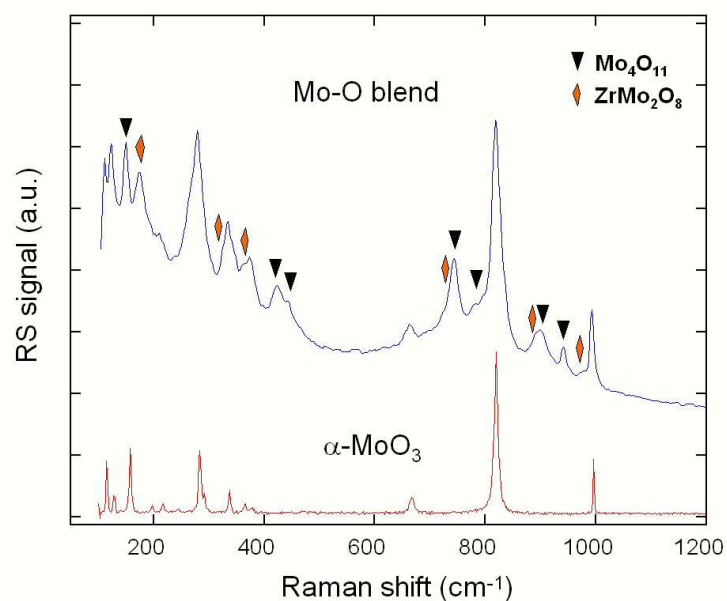


Figure 5. Raman spectra of the orthorhombic  $\alpha$ - $\text{MoO}_3$  and  $\text{ZrMo}_2\text{O}_8$ -decorated Mo-O blend. Samples were excited at a laser wavelength of 514.5 nm.

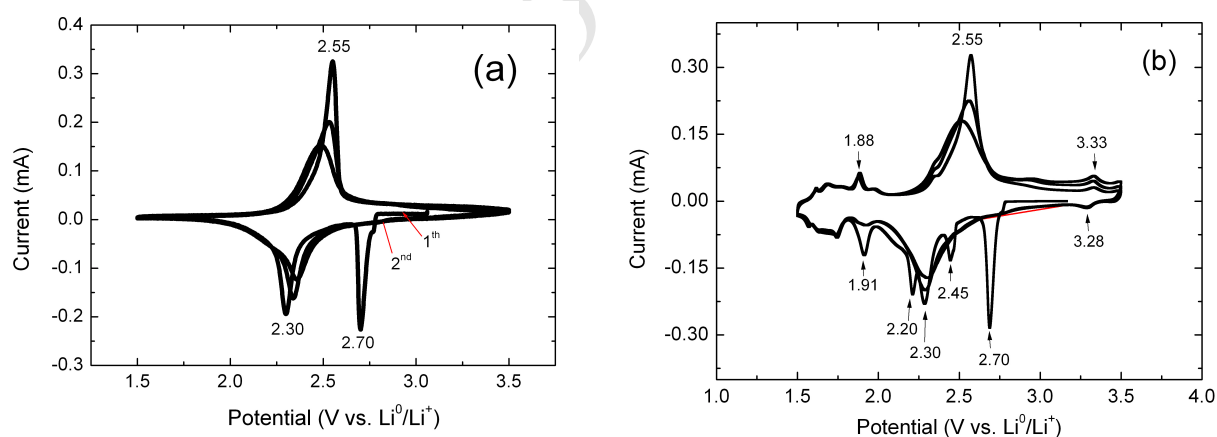


Figure 6. Cyclic voltammograms of  $\alpha$ - $\text{MoO}_3$  (a) and  $\text{MoO}_3$ - $\text{Mo}_4\text{O}_{11}$  blend (b) recorded at  $0.05 \text{ mV s}^{-1}$  in the potential range 1.5-3.5 V vs.  $\text{Li}^0/\text{Li}^+$  in Li cell using  $1 \text{ mol L}^{-1} \text{ LiPF}_6$  in EC:DEC electrolyte.

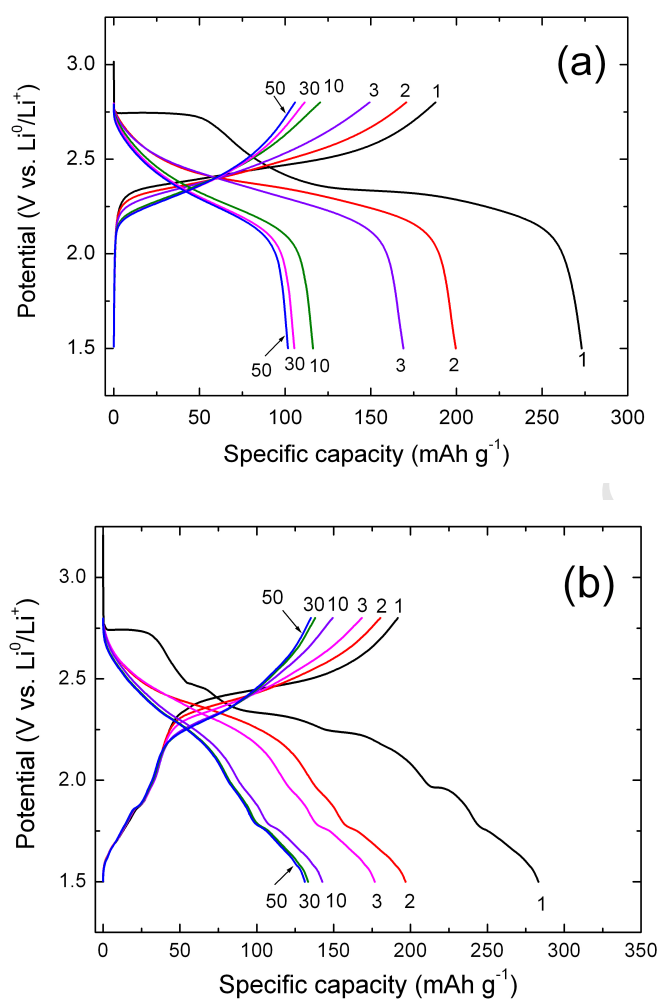


Figure 7. Charge-discharge profiles as a function of cycles of Li coin-type cells including (a)  $\alpha\text{-MoO}_3$  and (b)  $\text{MoO}_3\text{-Mo}_4\text{O}_{11}$  blend as cathode materials. Measurements were carried out at C/10 rate in the voltage range 1.5-2.8 V vs.  $\text{Li}^0/\text{Li}^+$ .

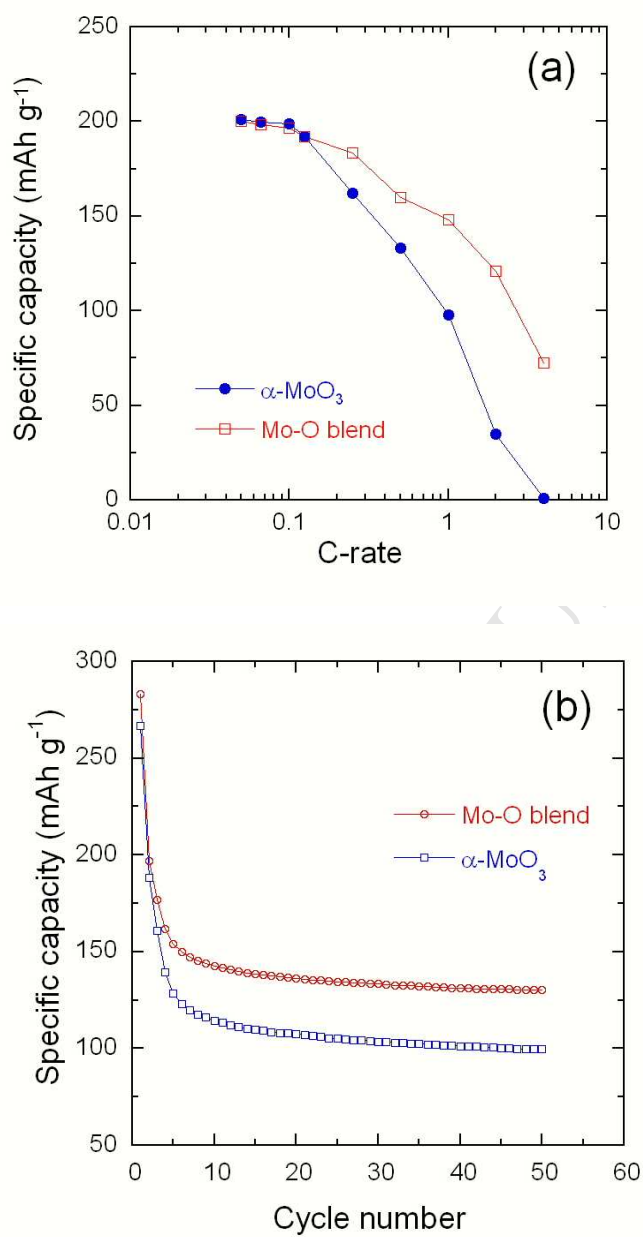


Figure 8. Electrochemical performance of Li cells with  $\alpha$ - $\text{MoO}_3$  and  $\text{MoO}_3$ - $\text{Mo}_4\text{O}_{11}$  blend electrodes: (a) rate capability (the rate is denoted C/n, where C is the theoretical cathode capacity and a full discharge occurs in n hours) and (b) cycling performance.

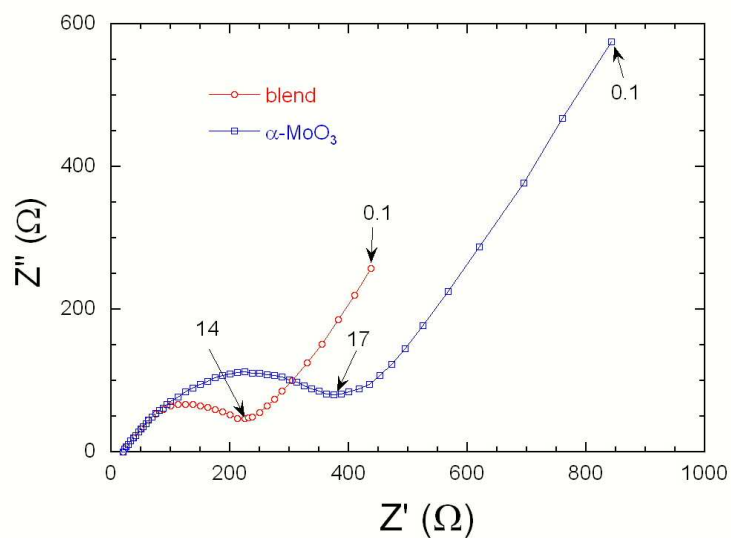


Figure 9. Nyquist plot of including (a)  $\alpha$ - $\text{MoO}_3$  and (b)  $\text{MoO}_3$ - $\text{Mo}_4\text{O}_{11}$  blend as cathode materials. Measurements were carried out in the 100 kHz-0.1 Hz frequency range with a 5 mV bias.

**Highlights**

- Oxygen deficient  $\text{Mo}_x\text{O}_y$  materials were synthesized by a citrate sol-gel method.
- The as-prepared materials exhibit an integrated-type blend structure decorated with  $\alpha\text{-ZrMo}_2\text{O}_8$  nanoparticles.
- Electrochemical features show the redox peaks attributed to distinct  $\text{Li}^+$ -ion insertion/extraction reactions in the  $\text{MoO}_3$  and  $\text{Mo}_4\text{O}_{11}$  hosts.
- Cyclic performance revealed improved reversibility and electrochemical stability of the composite.